Spontaneous Wetting Induced by Contact-Electrification at Liquid–Solid Interface

Zhen Tang, Dan Yang, Hengyu Guo, Shiquan Lin, and Zhong Lin Wang**

Wettability significantly influences various surface interactions and applications at the liquid–solid interface. However, the understanding is complicated by the intricate charge exchange occurring through contact electrification (CE) during this process. The understanding of the influence of triboelectric charge on wettability remains challenging, especially due to the complexities involved in concurrently measuring contact angles and interfacial electrical signals. Here, the relationship is investigated between surface charge density and change of contact angle of dielectric films after contact with water droplets. It is observed that the charge exchange when water spared lead to a spontaneous wetting phenomenon, which is termed as the contact electrification induced wetting (CEW). Notably, these results demonstrate a linear dependence between the change of contact angle (CA) of the materials and the density of surface charge on the solid surface. Continuous CEW tests show that not only the static CA but also the dynamics of wetting are influenced by the accumulation charges at the interface. The mechanism behind CEW involves the redistribution of surface charges on a solid surface and polar water molecules within liquid. This interaction results in a decrease in interface energy, leading to a reduction in the CA. Ab initio calculations suggest that the reduction in interface energy may stem from the enhanced surface charge on the substrate, which strengthens the hydrogen bond interaction between water and the substrate. These findings have the potential to advance the understanding of CE and wetting phenomena, with applications in energy harvesting, catalysis, and droplet manipulation at liquid–solid interfaces.

1. Introduction

Contact electrification (also known as triboelectrification) is a phenomenon that occurs at any interface when two objects come into contact and then separate, resulting in the triboelectric charge generation. The origin of the charges depends on the materials and specific experimental conditions, primarily divided into three types: ions, electrons, and material fragments transfer.[1] While the accumulation of charges on a surface may lead to potentially harmful discharges,[2] the sensible harnessing of surface charges offers a multitude of advantageous applications. These applications encompass electrophotography, dust removal, air purification, and more.[3] Electric sparks were produced when water droplets were swept away by steam escaping from a boiler, observed in 1840,[4] yet the utilization of charges generated at the liquid–solid interface remained rudimentary and faced numerous challenges. However, thanks to the discovery and widespread adoption of innovative technologies like Kelvin probe force microscopy (KPFM) for detecting surface charges, the foundational research on contact electrification (CE) has undergone a revival.[5] This renaissance in fundamental research has, in turn, propelled advancements in applications involving triboelectric charges. Recent interest has surged in CE, primarily because of its ability to initiate notable physical and chemical changes at the solid-liquid interface. For instance, charged inert solid materials exhibit exceptional catalytic activity in solution.[6] In addition, potential energy technologies based on charge transfer (e.g., triboelectric nanogenerator (TENG), hygroelectricity generator, and hydrovoltaic generator, etc.) have been developed and

Z. Tang, S. Lin, Z. L. Wang
Beijing Institute of Nanoenergy and Nanosystems
Chinese Academy of Sciences
Beijing 101400, P. R. China
E-mail: linshiquan@binn.cas.cn; zlwang@gatech.edu

Z. Tang, S. Lin, Z. L. Wang
School of Nanoscience and Technology
University of Chinese Academy of Sciences
Beijing 100049, P. R. China

D. Yang
State Key Laboratory of Organic-Inorganic Composites
College of Materials Science and Engineering
Beijing University of Chemical Technology
Beijing 100029, China

H. Guo
Department of Physics
Chongqing University
Chongqing 400044, China

Z. L. Wang
School of Materials Science and Engineering
Georgia Institute of Technology
Georgia, Atlanta 30332-0245, USA

**ADVANCED
SCIENCE NEWS**

www.advancedsciencenews.com

**ADVANCED
MATERIALS**

www.advmat.de

demonstrated efficient energy harvesting capabilities.[7] Furthermore, the dynamic of transport, spreading, and jump of droplets on a solid surface are all regulated by these charges.[8] Despite the pervasive effect of interface charges on the liquid–solid interface, there remains a significant gap in our knowledge of the intricate relationship between surface charge and wettability, which is a crucial scientific issue that needs to be thoroughly understood and explained.

Early observations revealed that water becomes electrified after flowing over an insulating film, accompanied by micro-discharge luminescence.[9] It was hypothesized that the origin of the electric charge on water droplets stemmed from the film. Further analysis of the membrane's surface potential indicated an uneven distribution of charge along the path of the flowing water droplet, with upstream sections consistently showing negative potential and downstream sections becoming positive.[10] Experiments have shown that upon contact with a solid, the surface charge does not be neutralized but transfers from the droplet to the solid surface.[11] Subsequent studies demonstrated that altering the ionic concentration of the droplet can change the amount of charge transferred between the solid and liquid. This transformation is attributed to the shielding effect of the charges.[12] Typically, surface charge generated by CE at the solid–liquid interface are often given less attention compared to the effect produced by strong external physical fields.[13] Recent research has shown that these surface charge influence how droplets move on surfaces and the control of droplet motion.[14] The movement of droplets across a charged film results in a decrease in the contact angle as the sliding distance increases, suggesting that dynamic wetting is influenced by surface charge.[15] Research on the surface tension changes of charged insulating films suggested that the contact angle might be influenced by surface charges.[16] However, establishing a clear link between dynamic wettability and surface charge is complex, primarily because of the challenges in measuring contact angle and interface electrical signal changes both simultaneously and in real-time. Consequently, the intricate relationship between CE and wettability continues to be only partially understood.

In this study, we utilized KPFM and contact angle goniometry to assess the surface potential and contact angles of various substrates following CE via contact with numerous water droplets. We found that the phenomenon of contact electrification induced wetting (CEW) significantly alters the wetting characteristics across a diverse range of materials, evidenced by variations in wetting behavior that span from 5° to 38°. This comprehensive study was carried out on 24 different materials, selected based on the established TENG database, which highlights the extensive applicability and significance of the CEW effect. Furthermore, we introduce an innovative approach to link the wetting behavior of materials with the surface charge generated during CE, by integrating a single electrode TENG with a goniometer. This novel method facilitates the simultaneous monitoring of dynamic changes in the contact angle (CA) and electrical signals, shedding light on the influence of accumulated surface charge on the dynamic wettability of materials. The linear relationship between CA and surface charge is indicates that the saturation of CA is likely due to surface charge saturation. The CEW consists of two stages: the accumulation of surface charge originating from CE, followed by wetting induction caused by these charges.

Molecular dynamics (MD) simulations have demonstrated that droplets exhibit smaller contact angles on charged surfaces, suggesting a more wettable interface. Moreover, Ab initio calculations provide evidence that this phenomenon can be attributed to enhanced hydrogen bond interactions between the water and the substrate. The mechanism behind the strengthened hydrogen bond interactions involves either a reduction in bond length or an increase in the number of hydrogen bonds. This finding holds great potential for developing new applications and technologies in charged surfaces and provides valuable insights into the field of wetting control and surface engineering.

2. Results and Discussion

2.1. Experimental Observation of the CEW

We used a custom-made droplet generator to study how triboelectric charge relate to material wettability when water droplets slide on a tilted dielectric surface (**Figure 1a**). Our apparatus allowed us to accurately observe and measure variations in contact angle (CA) and surface potential of the solid upon contact electrification with water droplets. Due to surface tension, a water droplet placed on a dielectric film spreads out and assumes a specific shape, as shown in Figure 1b. This shape is ultimately defined by the balance of surface tension forces acting on the solid surface. Upon reaching equilibrium, a distinct contact angle (θ) forms at the solid–gas–liquid interface, known as the CA. The wettability of a surface can be evaluated by its CA, with smaller angles indicating greater wettability or larger angles indicating lesser wettability. Materials are considered hydrophobic if θ is greater than 90°, and hydrophilic if θ is less than 90°.

It is commonly observed that when a water droplet moves across the surface of a dielectric material, it leaves behind residual charges on the surface. Particularly, solid materials with strong electronegativity like polytetrafluoroethylene (PTFE) tend to acquire negative charges when in contact with water droplets, while the droplets exhibit positive charges with the opposite sign. Surface charge generated by CE create an electric field gradient at the interface, leading to electrostatic attraction to both polar water molecules and ions,[17] which may impact the wetting of the solid surface (Figure 1c). To study this effect, changes in CA and surface potential of films were recorded using a CA goniometer and Kelvin probe force microscopy (KPFM), respectively. The experimental data showed a reduction in the hydrophobicity of the PTFE film, with the CA decreasing from 114° to 99° as the number of water droplets sliding across its surface increased from 0 to 1000 (Figure 1d). In addition, the surface potential of PTFE changed upon contact with different numbers of liquid droplets (Figure 1e), with KPFM analysis showing a gradual decrease from an initial positive 11 mV to a negative 663 mV, suggesting the accumulation of negative charges from the water after CE. Figure S1 (Supporting Information) demonstrates that the untreated PTFE surface initially displayed a mosaic distribution of positive and negative charges. As increased CE with droplets, a significant shift towards negative potential is observed on the PTFE samples, culminating in the accumulation of negative charges and the erasure of the mosaic pattern. This process is shown to enhance wettability, as the accumulated charges decrease the contact angle, directly affecting the surface's interaction with liquids.
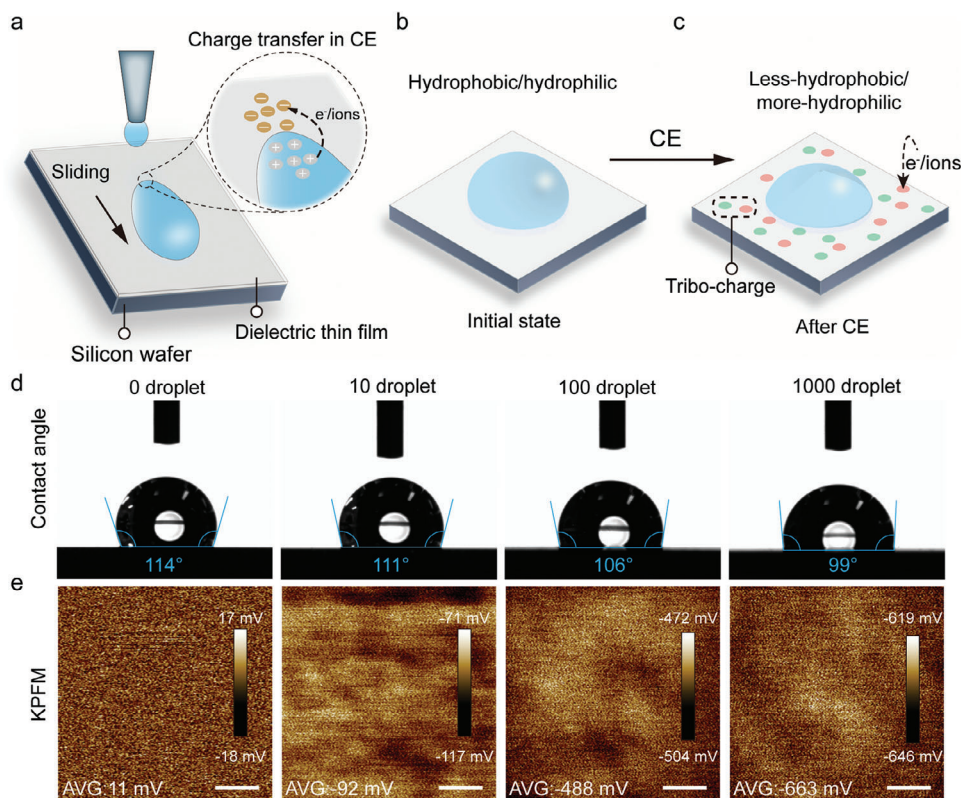
Figure 1. The concept of CEW. Schematic of the experimental setup. a) The inset shows a water droplet sliding across a dielectric thin film surface, where charge transfer occurs. b) Droplets on hydrophobic or hydrophilic solid surfaces at initial state. c) Spontaneous wetting behavior occurs when a dielectric thin film surface acquires surface charge from being in contact with water droplets. Images show d) the change in the CA and e) surface potential of a solid after contact with different numbers of droplets. Droplet volume: 3 µL. Scale bar: 5 µm.

2.2. Material Selection Guided by the TENG Database

Ensuring the CEW effect's universality necessitates experimentation across a broad spectrum of materials. Yet, the criteria and processes for material selection in prior studies are often vague, complicating the task of comparing outcomes. Our study aims to address this issue by establishing clear selection criteria and documenting our methodology transparently, thereby facilitating more reliable comparisons across different research findings.[1,18] To address this issue, we propose a comprehensive material selection guideline based on the TENG database (**Figure 2**). The guideline covers a wide range of materials and their percentage of use, and includes statistical data collected from 2012 to 2020. In addition, it provides a percentage on how to source, prepare, and handle each of the materials in the 1408 articles. With this guideline, researchers can make informed decisions when selecting materials for their experiments. Note S1 (Supporting Information) provides additional details about the guideline.

According to the material guidelines, the two most commonly used dielectric materials are PTFE and polydimethylsiloxane (PDMS), accounting for 16.7% and 11.8% of all materials, respectively. PTFE is popular due to its strong electronegative properties in the triboelectric series and its ability to store charge,[18] while polydimethylsiloxane (PDMS) is frequently used due to its easy preparation and compatibility. Other materials, such as Al

(12.4%), Cu (8.7%), and fluorinated ethylene propylene (FEP) (5.5%), are presented in descending order in the diagram. Materials with a usage rate of less than 1% account for around 20%. Metals like Al and Cu are commonly used as positive friction materials (electron donors) because of their abundance and low cost. About 66% of raw materials were obtained commercially, while 34% were synthesized, with 71.7% used directly and 26.1% chemically or physically modified to meet experimental requirements. Especially, ICP-RIE is widely used to modify material surfaces (2.2%). Solid–solid interface dominates TENG research (94.3%), while liquid–solid interfaces receive inadequate attention (5.5%). Interfaces such as solid–gas and liquid–gas, etc., are still in the early stages of development (0.2%). The contact-separation mode is the most widely used work mode for TENG (58.8%), followed by single electrode mode (16.4%), freestanding layer mode (12.8%), hybrid/multiple mode (8.8%), and sliding mode (3.5%). The material selection guidelines serve as a valuable reference for studies in TENG, wetting, and other interface fields.

2.3. The Universality of CEW: Verification and Examination

To evaluate the universality of CEW, we prepared the 24 frequently utilized in liquid–solid interface studies as specified in the database. We ensured strict control over both the preparation
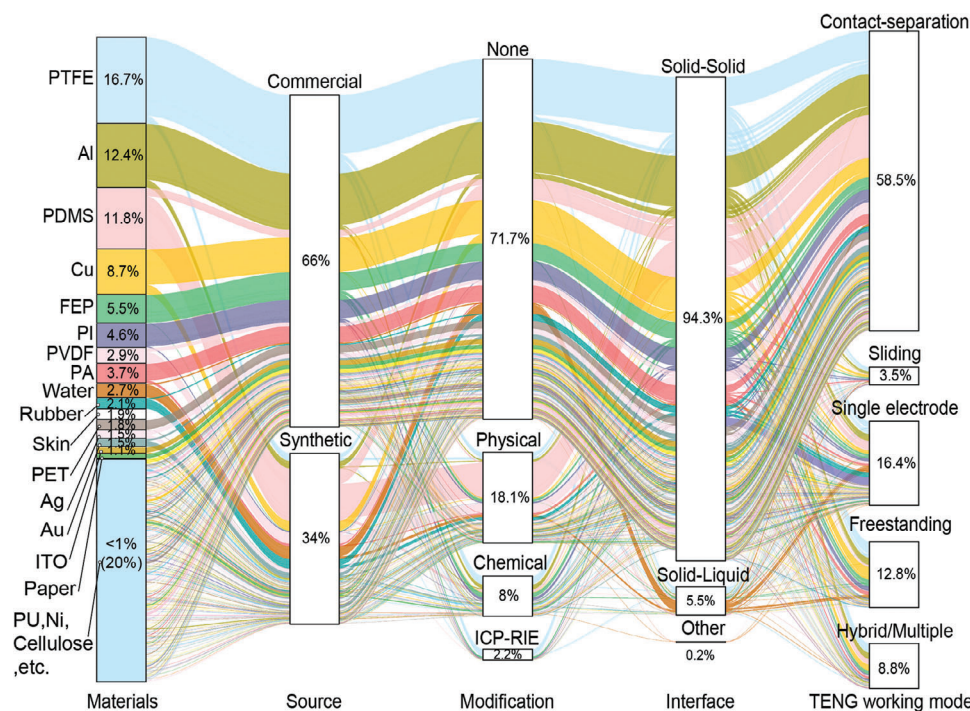
Figure 2. Overview of the guidelines for materials selection based on TENG database. The alluvial diagram illustrates the complete trajectory of materials from raw materials via processing and modification to the application at various interfaces and scenarios. Source data are provided as a source data file.

process and testing conditions to maintain consistency and reliability in our results (see Experimental Section; Figures S2 and S3, Supporting Information). Reproducibility was tested on three sample groups at 30-d intervals, showing a shift in CA of less than 1° (Figure S4, Supporting Information). All the films were charged with 1000 water droplets to achieve maximum surface charge saturation. In **Figure 3**a, it is evident that the change in contact angle (CA) varied among the materials, with the most significant change observed in epoxide (EP) and the smallest in polyvinylidene fluoride (PVDF), ranging from 5° to 38°. A linear correlation was observed between transferred charge density (TCD) and change in CA, except for PTFE and FEP which exhibited excessive charge density and fell beyond the predicted range (Figure 3b). The physical parameters of the different films, including film thickness d, relative permittivity ϵ, change in CA $\Delta\theta$, variation of roughness $\Delta Rq/Rq$, and change in surface potential $\Delta\varphi$, are shown in Table S1 (Supporting Information), respectively. All prepared films had nanometer-range thickness and low roughness, which was determined through atomic force microscopy (AFM), Figure S5 in the Supporting Information. We minimized the impact of substrate characteristics on film morphology by using ultra-smooth silicon wafers with roughness values less than 0.243 nm as substrates (Figure S6, Supporting Information). The morphology of the film surface was analyzed also using AFM, and all materials, except for polyurethane (PU) and polystyrene (PS), had a root mean square roughness (Rq) of less than 0.8 nm. Scanning electron microscopy (SEM) and energy-dispersive X-ray (EDX)spectrum analysis revealed a uniform distribution of the chemical composition of the materials (Figure S7, Supporting Information). The impact of water droplets on the surface morphology of most films was almost negligible, as

evidenced by the small rate of change $\Delta Rq/Rq$ in the roughness of all films before and after CE (Figure S8, Supporting Information). Our findings indicate that CEW can influence the wetting behavior of materials significantly, within a range of 9–48%. This underscores CEW as a prominent and promising effect that demands consideration in future research and applications.

2.4. Dynamic Response of CEW

To better understand the dynamic process involved in the relationship between surface charge and variation in CA, we conducted simultaneous characterizations of both the CA and electrical properties by a developed single TENG, as shown in **Figures 4**, S9 and Movie S1 (Supporting Information). Initially, a water droplet placed on a pristine PTFE film substrate (unground) grew as more liquid is injected into it, as depicted in Figure 4a(i)–(iii). Then, as the liquid was extracted, the droplet volume gradually decreased, as shown in Figure 4a(iii)–(iv) During this process, the dynamics variation of the CA, corresponding to the charge exchange occurring at the liquid–solid interface, were recorded simultaneously, as illustrated schematically in Figure 4b. The motion of droplets on solid surfaces typically results in the formation of advancing θ_{Adv} and receding angle θ_{Rec} (Figure 4c). However, on substrates with surface charge, it is believed that those CA may differ. For surfaces that have surface charge present (Figure 4d), there is a postulated relationship between the angles as follows: $\theta q_{Rec} < \theta_{Rec} < \theta q_{Sta} < \theta_{Sta} < \theta q_{Adv} < \theta_{Adv}$. During a test cycle, including the droplet expansion and contraction process, the changes in contact angle (CA) and electrical signal are shown in Figure 4e. Results indicate that as liquid volume
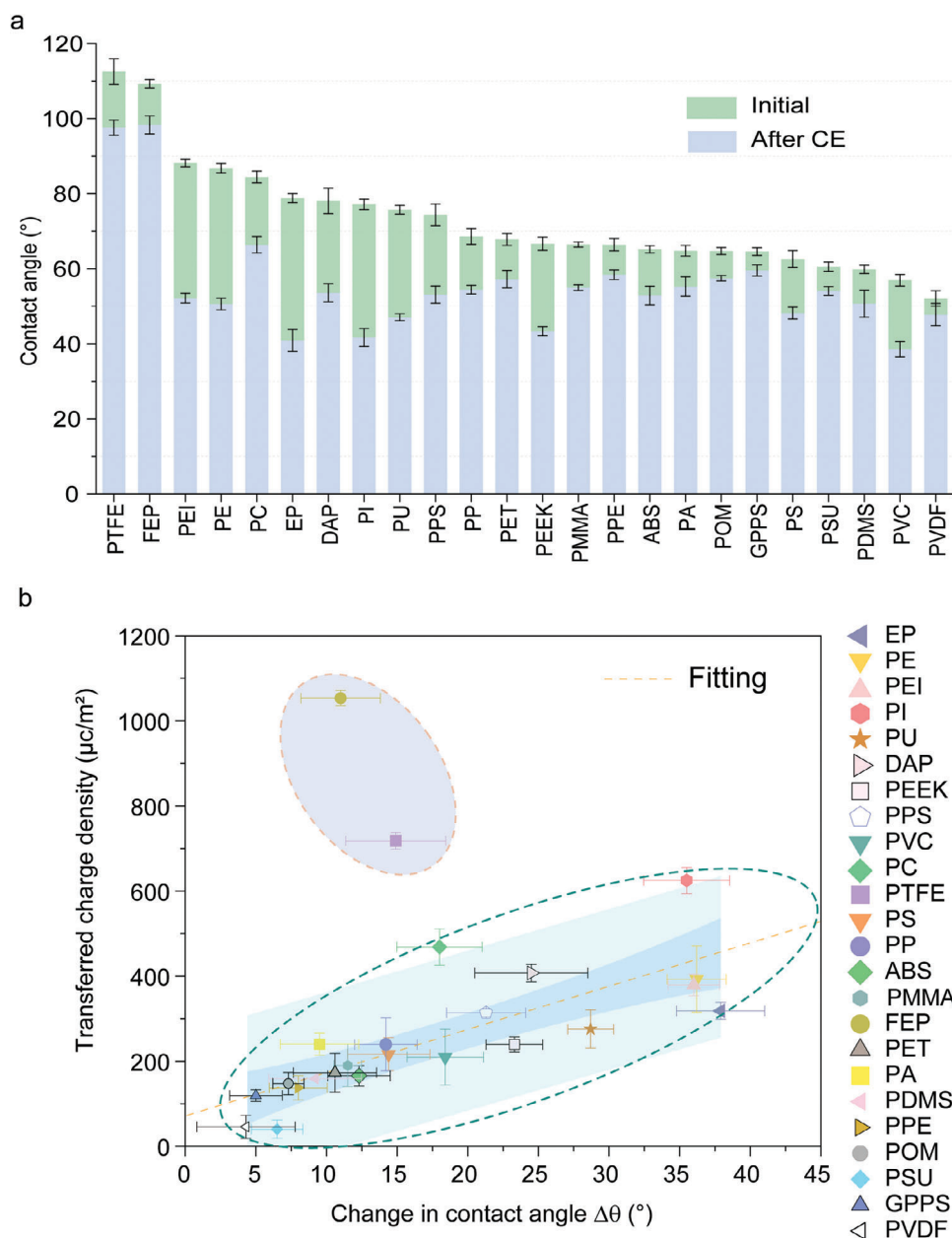
Figure 3. The effect of CEW on various materials. a) The change in the CA of materials before and after CE. Error bar represents standard deviation for twenty independent measurements. b) Transfer charge density as a function of the change in CA. The dark blue and light blue area represent the 95% confidence interval and 95% prediction interval, respectively. The area enclosed by the green dashed represents 91.6% of the data points. The Pearson correlation coefficient was 0.795, and the coefficient of determination was 0.633. Error bar represents standard deviation for ten independent measurements. The transfer of charge is in absolute value, according to Equation 2, the positive or negative sign does not affect the experimental results.

increases, CA, voltage, and charge also increase, while they decrease correspondingly when the liquid volume decreases. The changes in CA and voltage typically occur in the same direction, while the direction of charge is opposite, which aligns with the schematics shown in Figure 4a,b. The potential influence of precursor films might be mitigated by extremely low relative humidity, as evidenced by the lack of significant change in the signal during the extended duration of delay shown in Figure 4e. By varying the injected volume, the charge and voltage were observed to increase with liquid volume (Figure S10, Supporting

Information). This suggests that surface charge originate from CE that occur at the liquid–solid interface.

To simulate the dynamic wetting behavior of droplets on thin films, ten cycles tests were conducted to explore the impact of continuous charge accumulation on the dynamic change in CA (Figure 4f; Movie S2, Supporting Information). The slight CA fluctuation occurs just at the beginning of the first cycle, which we speculate is due to the fluctuation of the system energy caused by the charge exchange when the droplet first touches the solid surface and starts spreading, at which time the CA may

**ADVANCED
SCIENCE NEWS**

www.advancedsciencenews.com

**ADVANCED
MATERIALS**

www.advmat.de
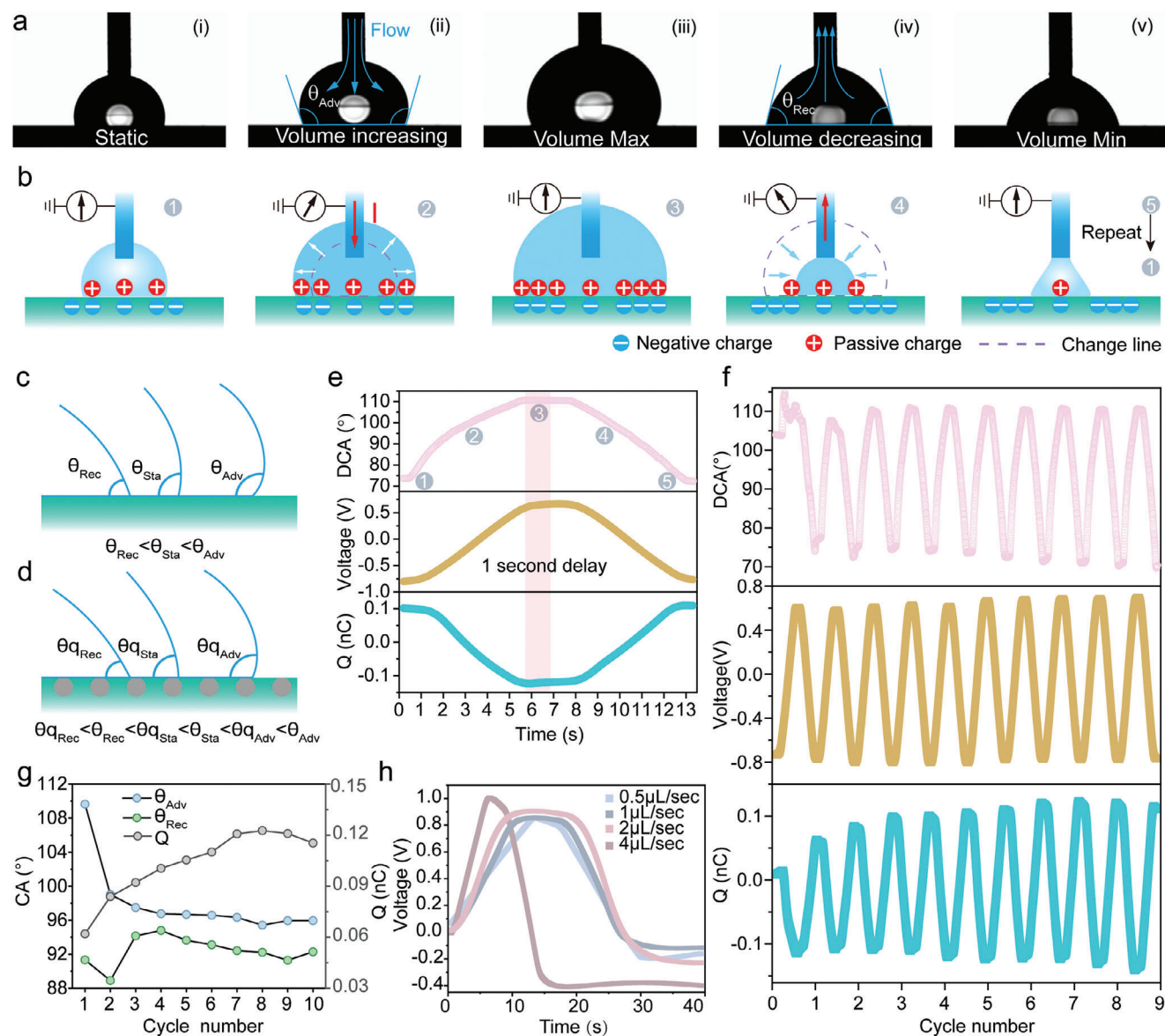
Figure 4. The effect of CEW on dynamic processes. a) Photograph of the droplet volume change process based on the needle method. Volume expansion of droplet due to syringe injection from (i) to (iii), but the volume decreases by needle extraction from (iii) to (v). Blue arrows represent the direction of water flow. b) The schematic diagram represents the charge transfer and current direction at the liquid–solid interface corresponding to the process in (a). The red arrow represents the direction of the electric current. Schematic diagram showing the static CA (θ_{Sta}), advancing angle (θ_{Adv}), and receding angle (θ_{Rce}) in the c) initial state and d) in after CE state. e) The revolution between CA and charge in a single cyclic test. f) Correspondence between dynamic variation of CA, voltage, and charge in ten cycles of testing. g) The cycle test curve for the change in dynamic CA, voltage, and charge. h) Voltage versus time under different liquid feed rate. In the schematic, the charge is positioned on a solid surface rather than being internal to the object.

be in a sub-stable state.[19] CE between solid and liquid, leading to the buildup of interface charges. This process results in a decrease in the minimum value of the contact angle. In repeated cyclic testing, a clear trend emerges, showing an increase in both charge and voltage amplitude, alongside a reduction in the minimum value of the dynamic change in contact angle. This implies that as droplets wet the thin film, simultaneous charge transfer takes place between the droplet and the substrate. When CE enhances wettability, wettability in turn enhances CE by increasing the contact area. Increased wetting cycles reveal the influence of charge transfer on the wetting process. Normally, droplet spread-

ing occurs spontaneously, indicating that the CEW phenomenon is self-triggered and does not require an external field. Furthermore, the periodicity of the interface signal curves remained stable throughout repeated tests, reinforcing the observation that dry conditions can significantly reduce the impact of precursor films on the measurements. We extract the relationship between the advancing and receding angles and the change of charge from tests cycle (Figure 4g). The increasing of surface charge leads to a decrease in the $\theta_{q_{Adv}}$ and a significantly greater impact compared to the $\theta_{q_{Rec}}$, confirming our hypothesis illustrated in Figure 4d. In other words, the contact hysteresis is affected by the

accumulated surface charge on the surface. The difference in the changes between the advancing and receding contact angles can be attributed to the advancing angle encountering stronger electrostatic forces than the receding angle. This occurs because the advancing angle moves towards newly charged surfaces, facing surface heterogeneities and energy shifts from charge transfer, which can disturb potential barriers and thus alter the advancing angle. In contrast, the receding angle withdraws from already wetted surfaces, where electrostatic forces and conditions are more stable, leading to minor changes in the CA. Thus, the advancing and receding angles are not solely determined by interface properties, but rather the charge exchange between the droplet and substrate also needs to be considered. This infer that the phenomenon of CEW may have a significant impact on the transport of droplets, as the lateral force exerted on the droplets is determined by differences in this parameter.[20]

The relationship between the flow rate of fluid injection and extraction and the corresponding voltage was examined (Figure 4h), and the slope of the voltage increase was determined to be proportional to the flow rate, indicating that the rapid spreading and contraction of the droplet contribute to the enhancement of the amount of charge transferred. Figure S11 and Movie S3 (Supporting Information) demonstrate that the interfacial electrical signal is affected by a delay in the contact line's movement. Additionally, it has been observed that an increase in the injection or withdrawal speed sharpens the slope of the voltage curve. This effect is attributed to the reduced duration of the delay. The effect of CEW has been demonstrated in different materials (Figure S12, Supporting Information). These findings suggest that the wetting behavior resulting from contact electrification originates from the spontaneous spread of liquid droplets on solid surfaces. Repeated wetting of the solid surface will highlight changes in both dynamic and static contact angles. Such spontaneous CEW could offer valuable insights and applications for regulating wetting. The suggested electrical signal detection method using the single electrode TENG shows potential for advancing interfacial sensing and energy harvesting.

2.5. The Mechanism of the CEW

CEW is commonly recognized as comprising two main steps: triboelectric charge generation through CE, and then triboelectric charge induce wetting (**Figure 5a**). When the solid surface comes into contact with a liquid during CE, surface charge are generated on the surface. The charge-storage capacity of the dielectric film allows these surface charge to persist on the surface for an extended duration. Upon placing a new droplet on the surface, the surface charge attracts ions and polar molecules in the water that carry opposite charges, resulting in the formation of an electric double layer (EDL) at the liquid–solid interface. Molecular dynamics (MD) simulations were employed to predict how droplets would wet PTFE substrates of different charged states (Figure 5b), as detailed in Note S4, Movies S4 and S5 in the Supporting Information. CE was mimicked by increasing the negative charges on fluorine atoms at the solid–liquid interface. Our findings show a significant reduction in the contact angle from 118° to 96°, as illustrated in Figure 5e. Ab initio calculations reveal a decreased distance in the O–H···F hydrogen bonds within

optimized adsorption structures of water molecules on charged polymer chains, highlighted in Figure 5c,d. These ab initio results suggest that the enhancement of intermolecular interactions, specifically through the O–H···F hydrogen bond, plays a crucial role in the observed decrease in interfacial tension.[21] Additionally, our study involved calculations on two distinct materials: polymethyl methacrylate (PMMA) and polydimethylsiloxane (PDMS) (Figure S13, Supporting Information). Notably, the selection of these materials was influenced by their unique interactions with water: PDMS acquires a positive charge, while PMMA gains a negative charge. Our ab initio calculations showed that for charged PMMA, the hydrogen bond lengths decreased, similar to PTFE, which was an expected outcome. In contrast, PDMS presented an unexpected scenario: the hydrogen bond length increased, driven by proton interactions, instead of decreasing. Moreover, the number of hydrogen bonds in PDMS increased from two to three, signifying an enhancement in proton-driven hydrogen bonding that aligns perfectly with the material characteristics. This enhancement in hydrogen bonding manifests in two forms: either through a reduction in bond lengths or an increase in the number of hydrogen bonds. Our findings align closely with experimental data, indirectly verifying the accuracy of the experimental results.

At the macroscopic scale, the continuously increasing surface charge on the insulating film cause the contact angle to decrease. In Figure 5f, we examined the relationship between the contact angles of PDMS and PTFE, two distinct materials prepared through different methods, while simultaneously measuring charge and voltage. We observed that as the surface potential increased from 0 to 10 V, the contact angles of all four films initially decreased significantly, reaching a certain point at which they stabilized. Above experimental results are in agreement with the simulated prediction Figure 5b. Contact angle saturation, was initially observed in the electrowetting. Currently, two models are employed to describe the connection between potential and contact angle changes under an applied electric field, the Young–Lippmann (Y–L) equation and the modified Y (m–Y) model:[22]

$$\cos\theta = \cos\theta_0 + \frac{\varepsilon_r\varepsilon_0 V^2}{2\gamma_{lv}d} \tag{1}$$

$$\cos\theta\,(V) = \cos\theta_0 + \frac{\varepsilon_r\varepsilon_0}{2\gamma_{lv}d}\left(V - V_0\right)^2 \tag{2}$$

where γ_{lv} represent liquid/gas interface tension, the θ_0 denotes the CA at normal conditions, θ denotes the CA under external applied potential V, d is the thickness of the dielectric film, ϵ_0 is the dielectric constant in the vacuum, and the ϵ_r is the relative permittivity, V_0 denotes the initial surface potential caused by surface charge (i.e., $\sigma_0 = \frac{\varepsilon_r\varepsilon_0 V_0}{d}$) are unknown and rely on the nonlinear response of the insulator material to the applied voltage, which posed challenges in detecting σ_0 in previous work.[22] The Y–L model, when parameterized using Equation (1), exhibited a discrepancy with our experimental results within the potential range of 0–10 V. Furthermore, it failed to fully capture the response of the CA as indicated by the horizontal long dashed line in Figure 5b. This collapse occurs because electrowetting often requires a high applied voltage when applying with micrometer-thick dielectric layers.[23] The CA of a material is
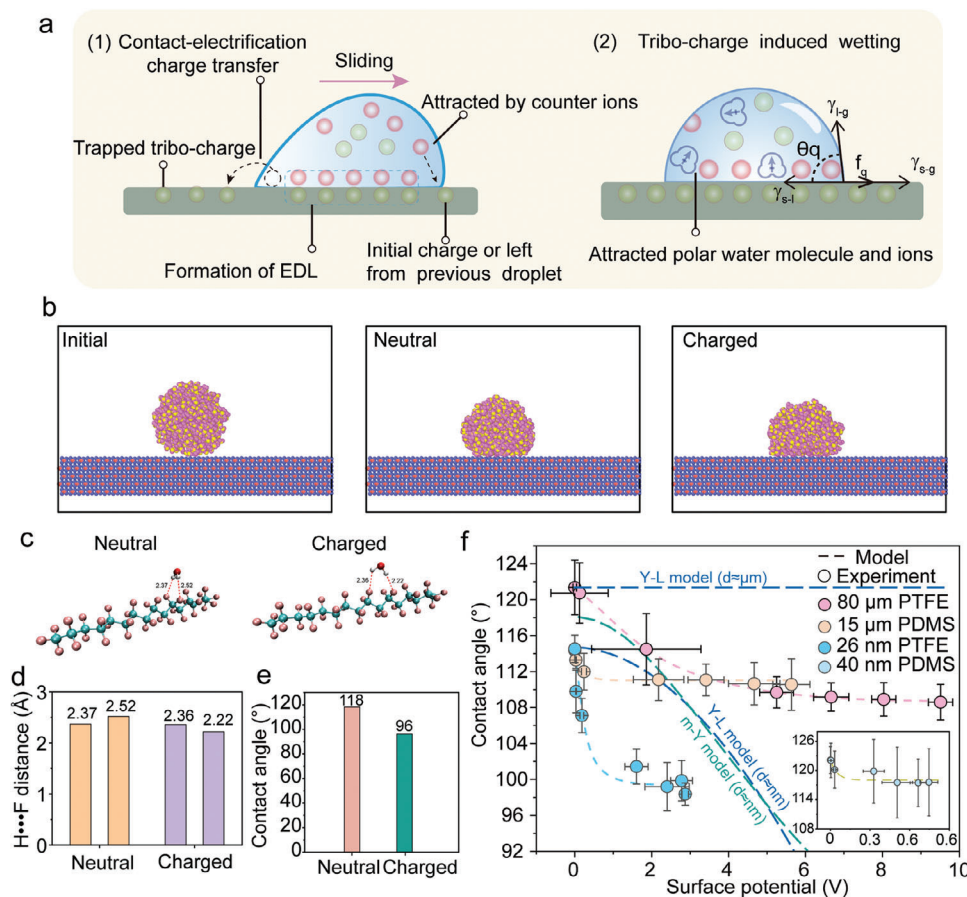
Figure 5. The mechanism and theoretical model of CEW. a) The schematic diagram illustrates that the CEW process consists of two steps: the charge accumulation process and the triboelectric charge-induced wetting. b) Snapshots of the simulated wetting process of water droplets on the different charged state surfaces of PTFE. c) Hydrogen bond calculation model in neutral and charged state. The dashed line represents hydrogen bonding. d) Hydrogen bond lengths and e) contact angle variation in different states. f) Comparison of theoretical models and experimental data for the change of CA on different surface potentials. Y–L mode is the Young–Lippmann model. Long dashed lines with accompanying text represent theoretical predictions based on various models with length-scale dependencies. The short-dashed line represents the exponential model fit. Error bar represents the standard deviation for ten independent measurements.

dependent on both voltage and thickness, and we propose reducing the thickness in Equation 1 by three orders of magnitude. According to the Y–L model and modified Y-model (Equation 2), CA undergoes a rapid decline as the potential increases, specifically at 6 V. At this voltage, experiments show CA reaches 92° and does not get saturation. The failure of the prediction in our experiment can be attributed to three factors: First, the electrostatic energy does not originate from the applied voltage but rather from the simultaneous accumulation of surface charge on the insulator's surface. Second, the system does not form a closed loop, rendering the Helmholtz flat capacitance model inapplicable. Third, the underlying principle governing the CEW phenomenon differs fundamentally from that of electrowetting. Moreover, CEW is influenced by intricate factors, such as the complexity of charge exchange occurrences, charge reversal at the hydrophilic–hydrophobic interface, and the valence of charged surface groups.[24] The nature of surface charge needs to be re-examined, and a single-electrode TENG was employed in our experiments to further analyze the surface charge. Remarkably, the Raman and Fourier transform infrared (FTIR) spectra exhibited

no discernible change in chemical composition before and after CE (Figures S14 and S15, Supporting Information), the slight variation observed in PDMS may be attributed to the sensitivity of the external agents.

Since we developed a single-electrode TENG capable of recording interfacial charges to overcome this drawback in electrowetting systems, we interestingly found, the surface charge demonstrated an exponential relationship with the number of droplets (Figure S16, Supporting Information), consistent with prior research.[7,25] Furthermore, this trend shows a mirror symmetry in comparison to the data presented in Figure 5b. This finding suggests an underlying relationship between the variation of contact angle with potential and the variation of charge with droplet number, both of which follow exponential equations. This implies a direct correlation between contact angle and charge. Consequently, the relationship between CA and surface charge is represented in a replotted graph (Figure S17, Supporting Information). The decrease in contact angle on the dielectric surface depends on the corresponding increase in surface charge, and both reach saturation simultaneously. More importantly, the

experimental results align with those obtained for various materials as shown in Figure 3b. The change in CA is proportional to the tribo-charge and follows an exponential relationship with time, which can be described by the following empirical equation:

$$\Delta\theta \propto k\sigma \cong \sigma_t e^{-at} + \sigma_i \tag{3}$$

where k is the efficient area, σ is surface charge density, a is accumulation coefficient, which depends on the electronegativities, σ_i is initial charges density, and σ_t is transferred charges density can be obtained by measurement, t is charging time. The fitting based on Equation 3, used for the data can predict the results of all experiments well (Figure 5f short dashed line). Our results suggest that the saturation phenomenon of the contact angle may be mainly due to the saturation of surface charge. Moreover, we believe that the detection of the surface charge or potential change through TENG can provide a preliminary indication of the wettability. This implies that the wettability of an object is at its lowest when the solid surface is nearly uncharged or electrically neutral. Conversely, when the solid is triboelectrified and the surface charge approaches saturation, wettability is highest.

3. Conclusions

Our study has established the widespread occurrence of the CEW phenomenon and its significant implications. Tasting 24 different materials strongly suggest a correlation between the change in contact angle and the surface charge. In other words, accumulation of surface charge on solid surface significantly reduces the contact angle. When CE enhances wettability, wettability in turn enhances CE by increasing the contact area. This suggests that detecting interfacial charge could partly serve as an indicator of wettability, potentially offering an innovative and noninvasive method for wetting sensors. This phenomenon may explain why the conventional droplet-based TENG demonstrates a rapid initial stage of exponential charge accumulation before reaching saturation. Additionally, the saturation of the contact angle observed in our experiments is likely due to the surface charge of the insulating film. We find that the saturation of surface charge hinders further charge exchange at the interface, potentially resulting in contact angle saturation. Our findings open up new avenues for investigating the interdiscipline of contact electrification and wetting, with potential applications not limited to solid-liquid systems but extending to wetting interfaces like gas–liquid and liquid–liquid. These discoveries hold significant promise in various fields, including energy conversion, regulating coffee stain effect,[26] droplet manipulation, microdroplet chemistry,[27] contact-electro-catalysis,[28] and superoleophobicity,[29] etc.

4. Experimental Section

Fabrication of the Dielectric Thin Film: The 4-inch Si wafer was first cut into 1 cm² squares using laser cutting and then cleaned by the RCA solutions to remove the oxide layer and impurities from the wafer surface, specific steps involved in these processes were shown in previous reports.[30] Cleaned silicon wafers were soaked in alcohol and then dried with nitrogen gas before use. Clean silicon wafers were placed in magnetron sputtering equipment (Discovery 635, Denton) and sputtered at a low power

setting. After the film and drops came into contact, films were dried using nitrogen gas and kept in a glove box. The 24 kinds of high-purity polymer targets used in the experiments were custom-made from ZhongNuo Advanced Material(Beijing)Technology Co., Ltd. P-type silicon wafers (resistivity 0.0015 Ω cm, 375 μm), commercial PTFE film (thickness: 80 μm, model: ASF-110, Zhongxing Huacheng) and PDMS film (thickness: 15 μm, model: PF-3-X4, Gel-pak) were purchased from Alibaba. The films were treated sequentially with acetone, alcohol, and deionized water via ultrasonic cleaning, and then dried using nitrogen gas. The raw materials used for the RCA solution such as H_2SO_4, HCl, and HF were purchased from Aladdin. Ultra-pure water (18.2 MΩ cm) was purified by a water purifier (Milli-Q Simplicity, Merck) and then sealed for use. A PDMS solution was obtained by mixing an elastomer base (Dow Corning 184) with a curing agent in a ratio of 10:1. The solution was then placed in a vacuum drying oven to remove dissolved air. Finally, the solution was mixed with dichloromethane at a volume ratio of 1:100 and stirred magnetically until it was clarified, resulting in a prep solution. The precursor solution is spin-coated on a silicon wafer at 2000–3000 rpm and then heated for 24 h to produce ultrathin PDMS films.

CA Measurements: The static CA was characterized by the sessile-drop method on a goniometer (OC25, Datephysics). The effect of the initial volume of the droplet on the CA of Si wafer was investigated (Figure S18, Supporting Information), to avoid the influence of gravity on the experiment, the capillary length $k^{-1} = \sqrt{\gamma/\rho g}$ was used to determine the Laplace force versus hydrostatic pressure, with the capillary force dominating the droplet's circular shape when the droplet radius R was less than k^{-1}. So, a 3 μL droplet was used for static CA measurements, and the droplet profile was fitted using the ellipse method in the SCA20 software. The advancing and receding angles were characterized using the needle method. A 3 μL droplet is first placed on the substrate, and a needle was inserted into the droplet to inject new liquid into it at a rate of 1 μL s⁻¹. The advancing angle was recorded as the droplet volume increased from 3 to 10 μL, and the receding angle is recorded as the volume decreases from 10 μL back to 3 μL. The entire process was recorded at 25 frames per second by a camera, with a one-second interval between injection and extraction. The quasi static CA cyclic test repeated the above process 10 times. The initial CAs of the control and RCA-treated silicon wafers were 40° and 26°, respectively (Figure S19, Supporting Information). For high experiment repeatability, all of the tests were conducted in a glove box with a high-purity nitrogen atmosphere (99.999%), where the environmental conditions were strictly controlled (temperature of 25±1 °C, chamber air pressure of 1 mbar, water and oxygen concentration less than 0.1 ppm).

Simultaneous Monitoring of Electrical Signals and Contact Angle: Additionally, we employed the seated drop method to measure the contact angle, whereby the sample was positioned on an insulated platform. Specifically, the metal needle of the syringe was connected to one end of the electrostatic meter 6517, while the other end was grounded. The solution inside the syringe was preneutralized. Furthermore, the solution pumping was accurately regulated using a stepper motor (Figures S9 and S20, Supporting Information).

Characterization of Chemical Composition: The micromorphology and chemical element distribution of the films were characterized using scanning electron microscopy (Nova Nano SEM 450) and energy dispersive X-ray spectroscopy (Raith/EDAX) at an accelerating voltage of 10 kV. Raman spectra of the samples were obtained with a Raman spectrometer (LABRAM HR EVOLUTION, HORIBA JY) using a 532 nm exciting wavelength, and the wave number range was from 50 to 4000 cm⁻¹. Fourier transform infrared spectra were obtained with an ATR-FTIR spectrometer (VERTEX80v, Bruker) to determine changes in the chemical structure. The spectral range for the FTIR spectrometer used was 4000 to 40 cm⁻¹. Samples were held in place by the clamp mechanism. All the tests were conducted in an ambient environment.

Relative Permittivity Measurement: The relative permittivity(ϵ_d)of the fabricated films was characterized by using a precision LCR meter (E4980A, Keysight). First, 100 nm gold was deposited on the surface of the film, and then a conductive tape was attached to form a sandwich-shaped capacitor. The flat plate method of testing is used to measure the dielectric constant of the capacitor. The two electrodes of the instrument

were clamped to the two ends of the capacitor, and the vector components of capacitance and dissipation were measured. The relative dielectric constant is then calculated using $\epsilon_d = \frac{Cd}{A\epsilon_0}$, where d is the thickness of the thin film, the values were shown in Table S1 (Supporting Information), and the A denotes the area, which is 1 cm^2, ϵ_0 denotes vacuum permittivity, which is 8.85×10^{-12} $F\,m^{-1}$.

CE for the Dielectric Films: The film charging procedure involved the utilization of a microinjector connected to a commercially available pump, and the metal needle at a distance of 0.5 cm from the film to minimize potential impact. The drops were dispensed slowly from the needle, which was grounded to shield against additional charges in the water. Each drop had an approximate volume of 10–15 µL. The ratio of inertial force to interface tension was evaluated using the We number = $\rho V^2 d/\gamma$ = 3.7, where ρ is the density of water with a value of 1000 kg m^{-3}, V represents the impact velocity at 0.3 m s^{-1}, d is the diameter of the droplet with a value of 3 mm, and γ represents the surface tension with a value of 72.8 mN m^{-1}.

The mechanism of TENG. The working principle of a single-electrode droplet TENG involves the conversion of droplet kinetic energy into electrical energy based on the effects of triboelectrification and electrostatic induction (shown in Figure S21 in the Supporting Information). When a droplet comes into contact with a thin film, charges are transferred from the droplet to the film, leaving an opposite charge within the droplet. As the droplet slides off the surface of the film, the metal electrode on the back of the film induces opposite charges to that on the surface of the film. The metal electrode is connected to an electrometer (Keithley 6517), which records the electrical signal.

Characterization for Surface Potential and Topography: All the experiments were performed on commercial atomic force microscopy (Multi-Mode 8, Bruker) using conductive tip (NSC18, MikroMasch, Au-coated, spring constant:2.8 N m^{-1}, frequency: 75kHz). The topographic image was scanned at a resolution of 256 lines, with a scan size of 5 µm × 5 µm and a scan frequency of 2 Hz in ScanAsyst mode. Kelvin probe force microscopy (KPFM) was used to measure the surface potential of thin films with a lift height of 50 nm in KPFM-AM mode. The average potential of an area of 5µm^2 was considered to be the potential of a point. The data acquired by the scan were collected from ten points in various locations. The thickness of the film was extracted from the scratches on the surface of the sample, and the data were processed using NanoScope Analysis software. The AFM experiments were conducted at 25 °C, atmospheric pressure, with a controlled relative humidity of 30% in a clean room.

The Calculation of Surface Charge Density: In the KPFM mode, a DC bias (V_{DC}) is applied to compensate for the contact potential difference (CPD) between the sample and the probe. The relationship between them can be expressed as follows:

$$V_{DC} + V_{CPD} - \frac{\sigma d}{\epsilon_d \epsilon_0} = 0 \tag{4}$$

where V_{DC} is the DC bias voltage applied to the probe, ϵ_0 is the dielectric constant in vacuum, and ϵ_d is the relative dielectric constant. d is the sample thickness. The relationship between charge density and potential can be obtained through the deformation of Equation 4 as follows:

$$\sigma = \frac{(V_{DC} + V_{CPD})\,\epsilon_d \epsilon_0}{d} \tag{5}$$

The transferred charge density (TCD) $\Delta\sigma$ can be expressed as:

$$\Delta\sigma = \sigma_{CE} - \sigma_{initial} = \frac{\Delta V \epsilon_d \epsilon_0}{d} \tag{6}$$

where $\sigma_{initial}$ is the initial charge density of the sample and σ_{CE} is the charge density of the sample after being charged by CE. Detailed discussions are in Note S2 in the Supporting Information.

Supporting Information

Supporting Information is available from the Wiley Online Library or from the author.

Conflict of Interest

The authors declare no conflict of interest.

Author Contributions

Z.L.W. and S.L. conceived and supervised the project. Z.T. designed and performed experiment. H.G. and D.Y. discussed the experiment and results. Z.T., S.L., and Z.L.W. wrote the manuscript. All authors discussed and reviewed the manuscript.

Data Availability Statement

The data that support the findings of this study are available from the corresponding author upon reasonable request.

Keywords

[1] a) M. Williams, *Am. Sci.* **2012**, *100*, 316; b) L. S. McCarty, G. M. Whitesides, *Angew. Chem., Int. Ed. Engl* **2008**, *47*, 2188; c) D. J. Lacks, R. M Sankaran, *J. Phys. D: Appl. Phys.* **2011**, *44*, 453001.

[2] J. Lowell, A. C. Rose-Innes, *Adv. Phys.* **1980**, *29*, 947.

[3] a) S. Panat, K. K. Varanasi, *Sci. Adv.* **2022**, *8*, eabm0078; b) D. M. Pai, B. E. Springett, *Rev. Mod. Phys.* **1993**, *65*, 163; c) H. Guo, J. Chen, L. Wang, A. C. Wang, Y. Li, C. An, J.-H. He, C. Hu, V. K. S. Hsiao, Z. L. Wang, *Nat. Sustain.* **2020**, *4*, 147.

[4] A. F. Anderson, *Electronics and Power* **1978**, *24*, 50.

[5] a) B. D. Terris, J. E. Stern, D. Rugar, H. J. Mamin, *Phys. Rev. Lett.* **1989**, *63*, 2669; b) V. Palermo, M. Palma, P. Samorì, *Adv. Mater.* **2006**, *18*, 145; c) H. T. Baytekin, A. Z. Patashinski, M. Branicki, B. Baytekin, S. Soh, B. A. Grzybowski, *Science.* **2011**, *333*, 308; d) H. T. Baytekin, B. Baytekin, T. M. Hermans, B. Kowalczyk, B. A. Grzybowski, *Science.* **2013**, *341*, 1368.

[6] a) Z. Wang, A. Berbille, Y. Feng, S. Li, L. Zhu, W. Tang, Z. L. Wang, *Nat. Commun.* **2022**, *13*, 130; b) Y. Wang, Y. Xu, S. Dong, P. Wang, W. Chen, Z. Lu, D. Ye, B. Pan, D. Wu, C. D. Vecitis, G. Gao, *Nat. Commun.* **2021**, *12*, 3508.

[7] a) W. Xu, H. Zheng, Y. Liu, X. Zhou, C. Zhang, Y. Song, X. Deng, M. Leung, Z. Yang, R. X. Xu, Z. L. Wang, X. C. Zeng, Z. Wang, *Nature.* **2020**, *578*, 392; b) Z. Zhang, X. Li, J. Yin, Y. Xu, W. Fei, M. Xue, Q. Wang, J. Zhou, W. Guo, *Nat. Nanotechnol.* **2018**, *13*, 1109; c) T. R. Ducati, L. H. Simoes, F. Galembeck, *Langmuir.* **2010**, *26*, 13763.

[8] a) Q. Sun, D. Wang, Y. Li, J. Zhang, S. Ye, J. Cui, L. Chen, Z. Wang, H.-J. Butt, D. Vollmer, X. Deng, *Nat. Mater.* **2019**, *18*, 936; b) N. Miljkovic, D. J. Preston, R. Enright, E. N. Wang, *Nat. Commun.* **2013**, *4*, 2517.

[9] M. Matsui, N. Murasaki, K. Fujibayashi, B. Peng You, Y. Kishimoto, *J. Electrostat.* **1993**, *31*, 1.

[10] K. Yatsuzuka, Y. Mizuno, K. Asano, *J. Electros.* **1994**, *32*, 157.

[11] A. Z. Stetten, D. S. Golovko, S. A. L. Weber, H. J. Butt, *Soft Matter.* **2019**, *15*, 8667.

[12] a) S. Sbeih, A. Luleci, S. Weber, W. Steffen, *Soft Matter.* **2024**, *20*, 558; b) J. Nie, Z. Ren, L. Xu, S. Lin, F. Zhan, X. Chen, Z. L. Wang, *Adv. Mater.* **2020**, *32*, 1905696.

[13] D. Brutin, V. Vancauwenberghe, P. Di Marco, in *Droplet Wetting and Evaporation* (Ed: D. Brutin), Academic Press, Aix-Marseille University, Marseille, France **2015**, pp. 413–425.

[14] a) X. Li, P. Bista, A. Z. Stetten, H. Bonart, M. T. Schür, S. Hardt, F. Bodziony, H. Marschall, A. Saal, X. Deng, R. Berger, S. A. L. Weber, H.-J. Butt, *Nat. Phys.* **2022**, *18*, 713; b) W. Xu, Y. Jin, W. Li, Y. Song, S. Gao, B. Zhang, L. Wang, M. Cui, X. Yan, Z. Wang, *Sci. Adv.* **2022**, *8*, eade2085.

[15] X. Li, A. D. Ratschow, S. Hardt, H.-J. Butt, *Phys. Rev. Lett.* **2023**, *131*, 228201.

[16] V. V. Yaminsky, M. B. Johnston, *Langmuir.* **1995**, *11*, 4153.

[17] Z. Tang, S. Lin, Z. L. Wang, *J. Phys. Chem. C.* **2022**, *126*, 8897.

[18] a) H. Zou, Y. Zhang, L. Guo, P. Wang, X. He, G. Dai, H. Zheng, C. Chen, A. C. Wang, C. Xu, Z. L. Wang, *Nat. Commun.* **2019**, *10*, 1427; b) J. A. Wiles, B. A. Grzybowski, A. Winkleman, G. M. Whitesides, *Anal. Chem.* **2003**, *75*, 4859; c) D. K. Davies, *J. Phys. D: Appl. Phys.* **1969**, *2*, 1533.

[19] A. Marmur, C. D Volpe, S. Siboni, A. Amirfazli, J. W. Drelich, *Surf. Innovations.* **2017**, *5*, 3.

[20] N. Gao, F. Geyer, D. W. Pilat, S. Wooh, D. Vollmer, H.-J. Butt, R. Berger, *Nat. Phys.* **2017**, *14*, 191.

[21] A. Luzar, S. Svetina, B. Žekš, *Chem. Phys. Lett.* **1983**, *96*, 485.

[22] a) B. Berge, *C. R. Acad. Sci., Ser. II.* **1993**, *317*, 157; b) F. Mugele, J.-C. Baret, *J. Phys.: Condens. Matter.* **2005**, *17*, R705.

[23] a) W. J. J. Welters, L. G. J. Fokkink, *Langmuir.* **1998**, *14*, 1535; b) M. Vallet, B. Berge, L. Vovelle, *Polymer.* **1996**, *37*, 2465.

[24] a) C. Calero, J. Faraudo, D. Bastos-Gonzalez, *J. Am. Chem. Soc.* **2011**, *133*, 15025; b) C. Calero, J. Faraudo, *Phys. Rev. E: Stat., Nonlinear, Soft Matter Phys.* **2009**, *80*, 042601; c) P. Ober, W. Q. Boon, M. Dijkstra, E. H. G. Backus, R. van Roij, M. Bonn, *Nat. Commun.* **2021**, *12*, 4102.

[25] F. Zhan, A. C. Wang, L. Xu, S. Lin, J. Shao, X. Chen, Z. L. Wang, *ACS Nano.* **2020**, *14*, 17565.

[26] H. B. Eral, D. M. Augustine, M. H. G. Duits, F. Mugele, *Soft Matter.* **2011**, *7*, 4954.

[27] a) B. Chen, Y. Xia, R. He, H. Sang, W. Zhang, J. Li, L. Chen, P. Wang, S. Guo, Y. Yin, L. Hu, M. Song, Y. Liang, Y. Wang, G. Jiang, R. N. Zare, *Proc. Natl. Acad. Sci. USA.* **2022**, *119*, 2209056119; b) M. A. Mehrgardi, M. Mofidfar, R. N. Zare, *J. Am. Chem. Soc.* **2022**, *144*, 7606.

[28] A. Berbille, X. F. Li, Y. Su, S. Li, X. Zhao, L. Zhu, Z. L. Wang, *Adv. Mater.* **2023**, *35*, 2304387.

[29] J. Yong, F. Chen, Q. Yang, J. Huo, X. Hou, *Chem. Soc. Rev.* **2017**, *46*, 4168.

[30] T. Ohmi, *J. Electrochem. Soc.* **1996**, *143*, 2957.